

A LARGE PLASTICITY DEFORMATION OF UNSATURATED SOIL FOR 3D DYNAMIC ANALYSIS OF LOWER SAN-FERNANDO DAM

A.R. Khoei^{*}, M. Anahid, M. Zarinfar, M. Ashouri and A. Pak
Center of Excellence in Structures and Earthquake Engineering,
Department of Civil Engineering, Sharif University of Technology,
P.O. Box. 11365-9313, Tehran, Iran

ABSTRACT

In this paper, a large plasticity deformation finite element modeling is presented for three-dimensional dynamic analysis of unsaturated soils with special reference to the failure of lower San Fernando dam under the 1971 earthquake. The finite element method is applied to the governing equations for the spatial discretization, followed by a generalized Newmark scheme used for the time domain discretization. Time stepping scheme is used in the fully implicit coupled method and a direct solution procedure is used for the coupled equation system. The framework of generalized plasticity is presented and the numerical results of unsaturated soils are demonstrated based on the Pastor-Zienkiewicz model (*Int. J. Numer. Analyt. Meth. Geomech.*, **14**: pp. 151–190, 1990), Bolzon-Schrefler-Zienkiewicz model (*Geotechnique*, **46**: pp. 279–289, 1996), and enhanced-BSZ model (*Transport in Porous Media*, **65**: pp.1–30, 2006). Finally, 3D dynamic analysis of the failure of lower San-Fernando dam is presented based on the modified Pastor-Zienkiewicz plasticity model.

Keywords: Unsaturated soil; plasticity model; large deformation; dynamic analysis; san fernando dam

1. INTRODUCTION

The mechanical behavior of the fully or partially saturated porous medium and in particular of soils, is governed largely by the interaction of solid skeleton with the pore fluid, generally water, present in the pore structure. This interaction is particularly strong in dynamic problems and may lead to liquefaction due to large pore pressure build up, which frequently occurs under earthquakes. Generally, porous media are described as the multiphase media with separate velocities and stresses for each phase, thereby the stress acting on the solid skeleton is usually referred to as effective stress, the hydrostatic stress acting on the fluid phase is denoted as the excess pore fluid pressure. The first theory of elastic wave

^{*} E-mail address of the corresponding author: arkhoei@sharif.edu (A.R. Khoei)

propagation in the fluid-saturated porous solid was developed by Biot [1, 2]. Although these first attempts were restricted to linear elastic soil skeleton and fluid flow through the solid phase governed by the Darcy law, they have been the basis for a lot of subsequent works in geophysics, soil and rock mechanics. A number of numerical modeling were reported for porous saturated media, including: the formulation based on soil displacements and pore pressures at low frequency, such as earthquakes [3–5], the material non-linearity behavior of the soil skeleton [6], and the liquefaction analysis of soil structures based on large deformation and nonlinear material behavior [7].

The theory of unsaturated soils was proposed based on the modification of Biot consolidation theory, which was initially developed for saturated soils. The original models were generally based on the typical simplifying assumptions; for instance, the rigid soil skeleton, passive gas phase (null gas flow and constant gas pressure equal to the atmospheric pressure), and omission of phase transitions which are basically in contrast with the physics of the problem in many situations. Chang and Duncan [8] postulated the pore water and pore air as a homogeneous and compressible fluid, in which the compressibility of the homogeneous fluid is expressed as functions of different parameters, such as pore water pressure and degree of saturation. An extension of two phase formulation to semi-saturated problems was proposed by Zienkiewicz et al. [9], in which the air or gas phase is assumed at atmospheric pressure. The model was employed in the dynamic analysis of semi-saturated dam under earthquake loading. The fully coupled dynamic models were presented for multi-phase fluid flow in deformable porous media involving the air and water phases in soils [10–14]. However, because of great complexity of multi-phase models, extensive and specially designed soil testing is required to determine the properties of the soil-air-water mixture.

Most of geomaterials under normal engineering conditions presents a mechanical behavior which depends on the level of stress, pore pressure, past history, direction of load increment and material structure. The plasticity based theory is then applied to provide a consistent framework in which the behavior can be accurately predicted. A generalized plasticity constitutive model was developed by Pastor et al. [15] to predict the basic phenomena encountered in dynamic loading of fully saturated porous media, such as the accumulation of plastic strain and pore pressure build-up during the loading process. This generalized plasticity does not require the yield and plastic potential surfaces, and the hardening modulus would be different in loading and unloading, which is particularly useful for cyclic loading. Thus, the model is in principle capable of representing the mechanical behavior of both dense and loose sands under quasi-static and dynamic loadings and can be used in several situations, such as the analysis of liquefaction, material softening and strain localization. The Pastor-Zienkiewicz model was extended by Bolzon et al. [16] to consider soil stiffness changes with suction. The Bolzon-Schrefler-Zienkiewicz (BSZ) model was applied to various problems, including: the compaction of gas reservoir [17], the strain localization of partially saturated clays and sands [18, 19], and the partially saturated soil dynamic of surface subsidence above an exploited gas reservoir [20]. The BSZ model was then extended by Santagiuliana and Schrefler [21] to consider the hydraulic constitutive relationship, hydraulic hysteresis, and a new term of plastic strain to account for irreversible deformation during cyclic drying and wetting until structural collapse.

In the present paper, the 2D dynamic analysis of porous saturated–unsaturated media

presented by Khoei et al. [22, 23] is extended into 3D large plasticity deformation of unsaturated soils. The numerical solution is based on the large FE deformation for spatial discretization, the generalized Newmark scheme for time discretization, and the generalized plasticity models, which include the Pastor-Zienkiewicz (PZ), the Bolzon-Schrefler-Zienkiewicz (BSZ), and the enhanced-BSZ models. Finally, the 3D dynamic analysis of the failure of lower San Fernando dam is presented based on the modified pastor-Zienkiewicz model.

2. MECHANICAL DESCRIPTION OF POROUS MEDIA

2.1 Governing equations of saturated soils

The essence of mathematical theory governing the behavior of porous media with a single pore fluid was first established by Biot [1, 2]. Assuming that the size of solid grains and pores are very small compared with the dimensions in macroscopic scale, the use of averaged variables for total stress σ_{ij} , solid matrix displacement u_i , and the mean flow velocity relative to the solid phase v_i are allowed. The effective stress is an essential concept defining the stresses, which control strength and constitutive behavior of porous material. Considering σ_{ij} as the total stress vector, δ_{ij} as the Kronecker delta and p as the pore fluid pressure with positive value in compression, the effective stress σ'_{ij} is defined by $\sigma'_{ij} = \sigma_{ij} - \alpha \delta_{ij} p$, in which α depends on the material type defined by $\alpha = 1 - K_{av}/K_s$, with K_s denoting the bulk modulus of solid particles and K_{av} the average bulk modulus of the solid skeleton.

The overall equilibrium equations of saturated porous media, particularly soils, with a single fluid phase, generally water are presented based on the total equilibrium for soil-pore fluid mixture, the equilibrium equation for the pore fluid, called the generalized Darcy equation, and the mass balance of flow equation [7]. The governing equations for the soil-fluid mixture can be written as

$$\sigma_{ij,j} + \rho \ddot{u}_i + \rho_f [\dot{v}_i + v_j v_{i,j}] - \rho b_i = 0 \quad (1)$$

$$p_{,i} + V_i^D + \rho_f \ddot{u}_i + \rho_f [\dot{v}_i + v_j v_{i,j}] / n - \rho b_i = 0 \quad (2)$$

$$-v_{i,i} + \dot{\varepsilon}_{ii} + \frac{n\dot{p}}{K_f} + \frac{(1-n)\dot{p}}{K_s} - \frac{K_{av}}{K_s} \left(\dot{\varepsilon}_{ii} + \frac{\dot{p}}{K_s} \right) + n \frac{\dot{\rho}_f}{\rho_f} + \dot{\theta} = 0 \quad (3)$$

where b_i is the body force per unit mass, ρ_f is the fluid density and ρ is the density of total composite, defined by $\rho = n\rho_f + (1-n)\rho_s$, with n denoting the porosity and ρ_s the density of solid particles. V_i^D represents the viscose drag force, which can be obtained from the Darcy seepage law by $v_i = k_{ij} V_j^D$, where k_{ij} is the dynamic permeability. In above equations, ε_{ij} are the total strains and K_f is the fluid bulk modulus. The definition of the

combined compressibility of the fluid and solid phases is defined by $C = nC_f + (\alpha - n)C_s$, in which C_f is the compressibility of fluid defined by $C_f = 1/K_f$, and C_s is the compressibility of solid particles defined by $C_s = 1/K_s$.

In equation (1), the underlined term is the effect of fluid relative acceleration to the solid particles and convective terms of this acceleration. Equation (2) ensures the momentum balance for the fluid phase and equation (3) indicates the mass balance of the fluid flow. In equation (3), the fluid flow divergence is balanced by the change of pores volume in the control volume. First term is the fluid flow divergence, second is the volume change due to change in strains, third is the additional storage volume due to compression of fluid under its pressure, forth is the additional storage volume due to compression of solid particle under fluid pressure, and fifth is the volume change of solid particles under their effective inter-granular stress. The last two terms are corresponding to change of fluid density and volume change of solid particles in the case of thermal changes and in general are negligible.

Equations (1)–(3) present the behavior of porous media in both static and dynamic conditions, with considering the interaction of its solid skeleton with the pore fluid. The pore fluid pressure p , the relative velocity of fluid flow to solid phase v_i and the displacement of solid skeleton u_i are the unknown variables in these equations system. When the acceleration frequencies are low, as in the case of earthquake motions, the underlined terms in above equations are not important and can be omitted [7]. By omitting these terms, the variable v_i can be eliminated from the equations, so the simplified governing equations, which contain two independent variables u_i and p , can be achieved as

$$\sigma_{ij,j} + \rho \ddot{u}_i - \rho b_i = 0 \quad (4)$$

$$\left[k_{ij} (p_{,j} + \rho_f \ddot{u}_j - \rho_f b_j) \right]_{,i} + \alpha \dot{\epsilon}_{ii} + \frac{\dot{p}}{C} = 0 \quad (5)$$

in which equations (4) and (5) together form the $\mathbf{u} - p$ formulation, which must be solved in a coupled manner.

2.2 Governing equations of unsaturated soils

In order to develop the governing equations of unsaturated media, some modifications must be applied to preceding section. In unsaturated conditions, the soil is taken as porous media in which the voids of porous media are filled partly by water and partly by air. Assuming the degrees of water and air saturation by S_w and S_a , respectively, in which $S_w + S_a = 1$, the density of soil-pore fluid mixture can be modified as $\rho = nS_w\rho_w + nS_a\rho_a + (1 - n)\rho_s$. Furthermore, the definition of effective stress can be modified based on the average pore pressure by applying the well known Bishop law as $p_{av} = \chi p_w + (1 - \chi)p_a$, with χ denoting the Bishop parameter depends on the degree of water saturation S_w . If the value of air pressure is set to zero ($p_a = 0$), the average pore pressure can be then approximated by $p_{av} \approx S_w p_w$.

In order to modify the mass balance equation of fluid flow, given in equation (3), the

divergence of fluid flow is balanced by the change of pores volume in the control volume. Considering the effect of water saturation along with a new term which take these changes into account, lead to

$$-v_{i,i} + \dot{\epsilon}_{ii} + S_w \left(\frac{n \dot{p}_w}{K_f} + \frac{(1-n) \dot{p}_w}{K_s} \right) - \frac{K_{av}}{K_s} \left(\dot{\epsilon}_{ii} + \frac{\dot{p}}{K_s} \right) + n \frac{\dot{p}_w}{\rho_w} + \dot{\theta} + n \dot{S}_w = 0 \quad (6)$$

A modified definition of the combined compressibility C can be written as $C^* = S_w(nC_f + (\alpha - n)C_s) + n\dot{S}_w/\dot{p}_w$. Applying the material parameter α and the new definition of combined compressibility C^* and then, omitting the negligible terms in equation (6), the following relation can be obtained

$$-v_{i,i} + \alpha \dot{\epsilon}_{ii} + \frac{\dot{p}_w}{C^*} + n S_w \frac{\dot{p}_w}{\rho_w} = 0 \quad (7)$$

in which the relation between the degree of saturation and permeability and also, the degree of saturation and water pressure must be taken into account.

Finally, the modified $\mathbf{u} - p$ formulation, including the total equilibrium of soil mixture and the continuity and mass balance equation, for static and dynamic behavior of saturated and unsaturated soils can be rewritten as

$$\sigma_{ij,j} + \rho \ddot{u}_i - \rho b_i = 0 \quad (8)$$

$$\left[k(p_{w,j} + S_w \rho_f \ddot{u}_j - S_w \rho_f b_j) \right]_{,i} + \alpha \dot{\epsilon}_{ii} + \frac{\dot{p}_w}{C^*} = 0 \quad (9)$$

3. NUMERICAL SOLUTION OF GOVERNING EQUATIONS

3.1 Finite element formulation

In order to obtain a numerical solution for the governing equations of saturated-unsaturated porous media, presented in previous section, a suitable discretization process is necessary for both spatial and time discretization. The spatial discretization can be achieved by shape functions for two variables u_i and p_w , defined as $\mathbf{u} = \mathbf{N}_u \bar{\mathbf{u}}$ and $p_w = \mathbf{N}_p \bar{\mathbf{p}}$, where \mathbf{N}_u and \mathbf{N}_p are the shape function of displacement and pore pressure fields. The governing equations can now be transformed into a set of algebraic equations in space by the use of an appropriate Galerkin method. The discretization of first equation in space can be achieved by pre-multiplying equation (8) by \mathbf{N}_u^T and integrating over the spatial domain as

$$\mathbf{M} \ddot{\bar{\mathbf{u}}} + \int_{\Omega} \bar{\mathbf{B}}^T \boldsymbol{\sigma}' d\Omega - \mathbf{Q} \bar{\mathbf{p}} - \mathbf{f}^{(1)} = 0 \quad (10)$$

where the mass matrix \mathbf{M} , the coupling matrix \mathbf{Q} , and the load vector $\mathbf{f}^{(1)}$ are defined as

$$\begin{aligned}\mathbf{M} &= \int_{\Omega} \mathbf{N}_u^T \rho \mathbf{N}_u d\Omega \\ \mathbf{Q} &= \int_{\Omega} \bar{\mathbf{B}}^T S_w \mathbf{m} \mathbf{N}_p d\Omega \\ \mathbf{f}^{(1)} &= \int_{\Omega} \mathbf{N}_u^T \rho \mathbf{b} d\Omega + \int_{\Gamma_t} \mathbf{N}_u^T \mathbf{t} d\Gamma\end{aligned}\tag{11}$$

and $\bar{\mathbf{B}}$ is the well known strain matrix relating the increments of strain and displacement (i.e. $d\boldsymbol{\varepsilon} = \bar{\mathbf{B}} d\bar{\mathbf{u}}$). The bar suffix is added as, if displacements are large, the strains depend non-linearly on displacements and the matrix $\bar{\mathbf{B}}$ is dependent on $\bar{\mathbf{u}}$. In the second term of equation (10), the constitutive law with respect to the incremental stress can be defined as

$$d\sigma'_{ij} = D_{ijkl}(d\varepsilon_{kl} - d\varepsilon_{kl}^0) + \sigma'_{ik} d\omega_{kj} + \sigma'_{jk} d\omega_{ki}\tag{12}$$

where $d\varepsilon_{ij}$ and $d\omega_{kl}$ are the incremental values of strain and rotation, respectively. The last two terms account for the Zaremba–Jaumann rotational stress changes (negligible generally in small displacement computation). In equation (12), D_{ijkl} is the soil property matrix, defined by suitable state variables and the direction of the increment, and ε_{ij}^0 refers to strains caused by external actions such as temperature changes.

In a similar manner the second discretized equation is derived by pre-multiplying equation (9) by \mathbf{N}_p^T and integrating over the spatial domain as

$$\mathbf{Q}^T \dot{\bar{\mathbf{u}}} + \mathbf{H} \bar{\mathbf{p}} + \mathbf{C} \dot{\bar{\mathbf{p}}} - \mathbf{f}^{(2)} = 0\tag{13}$$

where

$$\begin{aligned}\mathbf{H} &= \int_{\Omega} \nabla \mathbf{N}_p^T k \nabla \mathbf{N}_p d\Omega \\ \mathbf{C} &= \int_{\Omega} \mathbf{N}_p^T \frac{1}{C^*} \mathbf{N}_p d\Omega\end{aligned}\tag{14}$$

$$\mathbf{f}^{(2)} = - \int_{\Omega} \mathbf{N}_p^T \nabla^T (k S_w \rho_f \mathbf{b}) d\Omega$$

3.2 Large FE deformation

The nonlinearities in analyses of porous media arise from two distinct sources; constitutive nonlinearities and geometric nonlinearities, the latter being due to large displacements. Whether the displacements, or strains, are large or small it is imperative that the equilibrium conditions between the internal and external forces have to be satisfied. For geometrically nonlinear behavior, we can select either a total or an updated Lagrangian coordinate system.

A general definition of strains, which is valid whether the displacements or strains are large or small, was introduced by Green and St. Venant. Based on Green strain tensor, the non-linear strain displacement relationship can be defined in terms of the infinitesimal and large displacement components as $\boldsymbol{\varepsilon} = \boldsymbol{\varepsilon}_L + \boldsymbol{\varepsilon}_{NL}$, with $\boldsymbol{\varepsilon}_L$ and $\boldsymbol{\varepsilon}_{NL}$ denoting the linear and nonlinear strains and for three-dimensional problems are defined as

$$\boldsymbol{\varepsilon}_L = \begin{Bmatrix} \frac{\partial u}{\partial x} \\ \frac{\partial v}{\partial y} \\ \frac{\partial w}{\partial z} \\ \frac{\partial v}{\partial x} + \frac{\partial u}{\partial y} \\ \frac{\partial w}{\partial y} + \frac{\partial v}{\partial z} \\ \frac{\partial u}{\partial z} + \frac{\partial w}{\partial x} \end{Bmatrix}, \quad \boldsymbol{\varepsilon}_{NL} = \begin{Bmatrix} \frac{1}{2} \left(\frac{\partial u}{\partial x} \right)^2 + \frac{1}{2} \left(\frac{\partial v}{\partial x} \right)^2 + \frac{1}{2} \left(\frac{\partial w}{\partial x} \right)^2 \\ \frac{1}{2} \left(\frac{\partial u}{\partial y} \right)^2 + \frac{1}{2} \left(\frac{\partial v}{\partial y} \right)^2 + \frac{1}{2} \left(\frac{\partial w}{\partial y} \right)^2 \\ \frac{1}{2} \left(\frac{\partial u}{\partial z} \right)^2 + \frac{1}{2} \left(\frac{\partial v}{\partial z} \right)^2 + \frac{1}{2} \left(\frac{\partial w}{\partial z} \right)^2 \\ \frac{\partial u}{\partial x} \frac{\partial u}{\partial y} + \frac{\partial v}{\partial x} \frac{\partial v}{\partial y} + \frac{\partial w}{\partial x} \frac{\partial w}{\partial y} \\ \frac{\partial u}{\partial y} \frac{\partial u}{\partial z} + \frac{\partial v}{\partial y} \frac{\partial v}{\partial z} + \frac{\partial w}{\partial y} \frac{\partial w}{\partial z} \\ \frac{\partial u}{\partial z} \frac{\partial u}{\partial x} + \frac{\partial v}{\partial z} \frac{\partial v}{\partial x} + \frac{\partial w}{\partial z} \frac{\partial w}{\partial x} \end{Bmatrix} \quad (15)$$

In small displacement theory, the general first order linear strain approximation is obtained by neglecting the quadratic terms. In equation (15), the nonlinear terms of strain $\boldsymbol{\varepsilon}_{NL}$ is defined as $\boldsymbol{\varepsilon}_{NL} = \frac{1}{2} \mathbf{A}_\theta \boldsymbol{\theta}$, with $\boldsymbol{\theta}$ denoting the displacement gradient and \mathbf{A}_θ a suitably defined matrix operator which contains displacement derivatives and can be derived from the definition of $\boldsymbol{\varepsilon}_{NL}$. For a set of virtual displacements, the corresponding virtual Green strains are given as $d\boldsymbol{\varepsilon} = d\boldsymbol{\varepsilon}_L + d\boldsymbol{\varepsilon}_{NL}$.

In order to complete the numerical solution of FE equations, it is necessary to integrate the differential equations (10) and (13) in time. The generalized Newmark GN22 method is employed for the displacement field and GN11 method for the pressure field as

$$\begin{aligned} \bar{\mathbf{u}}_{n+1} &= \bar{\mathbf{u}}_n + \Delta t \dot{\bar{\mathbf{u}}}_n + \left(\frac{1}{2} - \beta\right) \Delta t^2 \ddot{\bar{\mathbf{u}}}_n + \beta \Delta t^2 \ddot{\bar{\mathbf{u}}}_{n+1} = \bar{\mathbf{u}}_{n+1}^p + \beta \Delta t^2 \ddot{\bar{\mathbf{u}}}_{n+1} \\ \dot{\bar{\mathbf{u}}}_{n+1} &= \dot{\bar{\mathbf{u}}}_n + (1 - \gamma) \Delta t \ddot{\bar{\mathbf{u}}}_n + \gamma \Delta t \ddot{\bar{\mathbf{u}}}_{n+1} = \dot{\bar{\mathbf{u}}}_{n+1}^p + \gamma \Delta t \ddot{\bar{\mathbf{u}}}_{n+1} \end{aligned} \quad (16)$$

and

$$\bar{\mathbf{p}}_{n+1} = \bar{\mathbf{p}}_n + (1 - \theta) \Delta t \dot{\bar{\mathbf{p}}}_n + \theta \Delta t \dot{\bar{\mathbf{p}}}_{n+1} = \bar{\mathbf{p}}_{n+1}^p + \theta \Delta t \dot{\bar{\mathbf{p}}}_{n+1} \quad (17)$$

where parameters β , γ and θ are in the range of 0 to 1 and for unconditional stability of the solution process $\beta \geq 1/4$, $\gamma \geq 1/2$ and $\theta \geq 1/2$ [24]. It is assumed that the variables are known at time t_n and should be evaluated at time $t_{n+1} = t_n + \Delta t$, in which the only unknown

variables are $\ddot{\mathbf{u}}_{n+1}$ and $\dot{\mathbf{p}}_{n+1}$. Substituting relations (16) and (17) into equations (10) and (13) at time t_{n+1} , we obtain

$$\begin{aligned}\mathbf{G}_{n+1}^{(1)} &= (\mathbf{M}_{n+1} + \beta \Delta t^2 \widehat{\mathbf{K}}_{n+1}) \ddot{\mathbf{u}}_{n+1} - (\theta \Delta t \mathbf{Q}_{n+1}) \dot{\mathbf{p}}_{n+1} + \mathbf{F}_{n+1}^{(1)} = \mathbf{0} \\ \mathbf{G}_{n+1}^{(2)} &= (\gamma \Delta t \mathbf{Q}_{n+1}^T) \ddot{\mathbf{u}}_{n+1} + (\theta \Delta t \mathbf{H}_{n+1} + \mathbf{C}_{n+1}) \dot{\mathbf{p}}_{n+1} + \mathbf{F}_{n+1}^{(2)} = \mathbf{0}\end{aligned}\quad (18)$$

or

$$\begin{Bmatrix} \mathbf{G}_{n+1}^{(1)} \\ \mathbf{G}_{n+1}^{(2)} \end{Bmatrix} = \begin{bmatrix} \mathbf{M}_{n+1} + \beta \Delta t^2 \widehat{\mathbf{K}}_{n+1} & -\theta \Delta t \mathbf{Q}_{n+1} \\ \gamma \Delta t \mathbf{Q}_{n+1}^T & \theta \Delta t \mathbf{H}_{n+1} + \mathbf{C}_{n+1} \end{bmatrix} \begin{Bmatrix} \ddot{\mathbf{u}}_{n+1} \\ \dot{\mathbf{p}}_{n+1} \end{Bmatrix} + \begin{Bmatrix} \mathbf{F}_{n+1}^{(1)} \\ \mathbf{F}_{n+1}^{(2)} \end{Bmatrix} = \begin{Bmatrix} \mathbf{0} \\ \mathbf{0} \end{Bmatrix}\quad (19)$$

where $\widehat{\mathbf{K}}_{n+1} \bar{\mathbf{u}} = \int_{\Omega} \bar{\mathbf{B}}_{n+1}^T \boldsymbol{\sigma}'_{n+1} d\Omega$, and the matrix $\bar{\mathbf{B}}$ can be written in terms of the linear and nonlinear strain-displacement matrix, i.e. $\bar{\mathbf{B}} = \mathbf{B}_L + \mathbf{B}_{NL}(\bar{\mathbf{u}})$, where \mathbf{B}_L is the same matrix as in a linear infinitesimal strain analysis and only \mathbf{B}_{NL} depends on the displacement. Taking the variation from $\boldsymbol{\varepsilon}_{NL} = \frac{1}{2} \mathbf{A}_{\theta} \boldsymbol{\theta}$ results in $d\boldsymbol{\varepsilon}_{NL} = \mathbf{A}_{\theta} d\boldsymbol{\theta}$, in which $\boldsymbol{\theta}$ is determined in terms of the Cartesian shape function derivatives \mathbf{G} and nodal parameter $\bar{\mathbf{u}}$, as $\boldsymbol{\theta} = \mathbf{G} \bar{\mathbf{u}}$. Hence, $d\boldsymbol{\varepsilon}_{NL} = \mathbf{A}_{\theta} \mathbf{G} d\bar{\mathbf{u}}$ and the nonlinear strain-displacement matrix can be defined as $\mathbf{B}_{NL} = \mathbf{A}_{\theta} \mathbf{G}$, i.e.

$$\mathbf{B}_L^I = \begin{bmatrix} \frac{\partial N_I}{\partial x} & 0 & 0 \\ 0 & \frac{\partial N_I}{\partial y} & 0 \\ 0 & 0 & \frac{\partial N_I}{\partial z} \\ \frac{\partial N_I}{\partial y} & \frac{\partial N_I}{\partial x} & 0 \\ 0 & \frac{\partial N_I}{\partial z} & \frac{\partial N_I}{\partial y} \\ \frac{\partial N_I}{\partial z} & 0 & \frac{\partial N_I}{\partial x} \end{bmatrix}, \quad \mathbf{B}_{NL}^I = \begin{bmatrix} \frac{\partial N_I}{\partial x} \frac{\partial u}{\partial x} & \frac{\partial N_I}{\partial x} \frac{\partial v}{\partial x} & \frac{\partial N_I}{\partial x} \frac{\partial w}{\partial x} \\ \frac{\partial N_I}{\partial y} \frac{\partial u}{\partial y} & \frac{\partial N_I}{\partial y} \frac{\partial v}{\partial y} & \frac{\partial N_I}{\partial y} \frac{\partial w}{\partial y} \\ \frac{\partial N_I}{\partial z} \frac{\partial u}{\partial z} & \frac{\partial N_I}{\partial z} \frac{\partial v}{\partial z} & \frac{\partial N_I}{\partial z} \frac{\partial w}{\partial z} \\ \frac{\partial N_I}{\partial x} \frac{\partial u}{\partial y} + \frac{\partial N_I}{\partial y} \frac{\partial u}{\partial x} & \frac{\partial N_I}{\partial x} \frac{\partial v}{\partial y} + \frac{\partial N_I}{\partial y} \frac{\partial v}{\partial x} & \frac{\partial N_I}{\partial x} \frac{\partial w}{\partial y} + \frac{\partial N_I}{\partial y} \frac{\partial w}{\partial x} \\ \frac{\partial N_I}{\partial y} \frac{\partial u}{\partial z} + \frac{\partial N_I}{\partial z} \frac{\partial u}{\partial y} & \frac{\partial N_I}{\partial y} \frac{\partial v}{\partial z} + \frac{\partial N_I}{\partial z} \frac{\partial v}{\partial y} & \frac{\partial N_I}{\partial y} \frac{\partial w}{\partial z} + \frac{\partial N_I}{\partial z} \frac{\partial w}{\partial y} \\ \frac{\partial N_I}{\partial z} \frac{\partial u}{\partial x} + \frac{\partial N_I}{\partial x} \frac{\partial u}{\partial z} & \frac{\partial N_I}{\partial z} \frac{\partial v}{\partial x} + \frac{\partial N_I}{\partial x} \frac{\partial v}{\partial z} & \frac{\partial N_I}{\partial z} \frac{\partial w}{\partial x} + \frac{\partial N_I}{\partial x} \frac{\partial w}{\partial z} \end{bmatrix}\quad (20)$$

and

$$[\mathbf{G}^I]^T = \begin{bmatrix} \frac{\partial N_I}{\partial x} & 0 & 0 & \frac{\partial N_I}{\partial y} & 0 & 0 & \frac{\partial N_I}{\partial z} & 0 & 0 \\ 0 & \frac{\partial N_I}{\partial x} & 0 & 0 & \frac{\partial N_I}{\partial y} & 0 & 0 & \frac{\partial N_I}{\partial z} & 0 \\ 0 & 0 & \frac{\partial N_I}{\partial x} & 0 & 0 & \frac{\partial N_I}{\partial y} & 0 & 0 & \frac{\partial N_I}{\partial z} \end{bmatrix}\quad (21)$$

The nonlinear coupled FE equations (19) can be solved using the Newton Raphson procedure for iteration i as

$$\begin{bmatrix} \frac{\partial \mathbf{G}^{(1)}}{\partial \ddot{\mathbf{u}}} & \frac{\partial \mathbf{G}^{(1)}}{\partial \dot{\mathbf{p}}} \\ \frac{\partial \mathbf{G}^{(2)}}{\partial \ddot{\mathbf{u}}} & \frac{\partial \mathbf{G}^{(2)}}{\partial \dot{\mathbf{p}}} \end{bmatrix}_{n+1}^i \begin{Bmatrix} d\ddot{\mathbf{u}}_n^i \\ d\dot{\mathbf{p}}_n^i \end{Bmatrix} = - \begin{Bmatrix} \mathbf{G}^{(1)} \\ \mathbf{G}^{(2)} \end{Bmatrix}_{n+1}^i \quad (22)$$

Finally, the tangential stiffness matrix $\hat{\mathbf{K}}_{n+1}$ can be obtained by taking the variation from $\int_{\Omega} \bar{\mathbf{B}}_{n+1}^T \boldsymbol{\sigma}'_{n+1} d\Omega$ as

$$\hat{\mathbf{K}}_{n+1}^i d\bar{\mathbf{u}}_n^i \equiv \left(\int_{\Omega} \bar{\mathbf{B}}^T d\boldsymbol{\sigma}' d\Omega \right)_{n+1}^i + \left(\int_{\Omega} d\bar{\mathbf{B}}^T \boldsymbol{\sigma}' d\Omega \right)_{n+1}^i \quad (23)$$

The above equation shows that the stiffness matrix $\hat{\mathbf{K}}$ consists of two parts; the first part involves the derivative of stress $d\boldsymbol{\sigma}'$, which depends on the material response and leads to the material tangent stiffness matrix $\mathbf{K}^{\text{material}}$, and the second part involves the current state of stress $\boldsymbol{\sigma}'$, which accounts for the geometric effects of the deformation (including rotation and stretching) and leads to the geometric stiffness matrix $\mathbf{K}^{\text{geometry}}$.

The material tangent stiffness matrix $\mathbf{K}^{\text{material}}$ can be obtained by substituting the constitutive law definition $d\boldsymbol{\sigma}' = \mathbf{D} d\boldsymbol{\varepsilon}$ and $d\boldsymbol{\varepsilon} = \bar{\mathbf{B}} d\bar{\mathbf{u}}$ into the first part of relation (23) as

$$\mathbf{K}^{\text{material}} = \int_{\Omega} \bar{\mathbf{B}}^T \mathbf{D} \bar{\mathbf{B}} d\Omega \equiv \mathbf{K}_L + \mathbf{K}_{NL} \quad (24)$$

where \mathbf{K}_L represents the usual, small displacement stiffness matrix and the matrix \mathbf{K}_{NL} is due to the large displacements. The geometric stiffness matrix $\mathbf{K}^{\text{geometry}}$ can be derived by substituting $d\bar{\mathbf{B}} = d\mathbf{B}_{NL} = d\mathbf{A}_{\theta} \mathbf{G}$ into the second part of relation (23) as

$$\mathbf{K}^{\text{geometry}} = \int_{\Omega} \mathbf{G}^T \mathbf{M}_{\sigma} \mathbf{G} d\Omega \quad (25)$$

where \mathbf{M}_{σ} is a 9×9 matrix of the six stress components for three-dimensional problems and is defined by

$$\mathbf{M}_{\sigma} = \begin{bmatrix} \sigma'_x \mathbf{I}_{3 \times 3} & \tau_{xy} \mathbf{I}_{3 \times 3} & \tau_{xz} \mathbf{I}_{3 \times 3} \\ & \sigma'_y \mathbf{I}_{3 \times 3} & \tau_{yz} \mathbf{I}_{3 \times 3} \\ sym. & & \sigma'_z \mathbf{I}_{3 \times 3} \end{bmatrix} \quad (26)$$

where \mathbf{I} is the identity matrix. Thus, the total tangential stiffness matrix $\hat{\mathbf{K}}$ used in nonlinear coupled FE equations (19) is defined as

$$\hat{\mathbf{K}}_{n+1}^i = \left(\int_{\Omega} \bar{\mathbf{B}}^T \mathbf{D} \bar{\mathbf{B}} d\Omega \right)_{n+1}^i + \left(\int_{\Omega} \mathbf{G}^T \mathbf{M}_{\sigma} \mathbf{G} d\Omega \right)_{n+1}^i \quad (27)$$

All the ingredients necessary for computing the large deformation of saturated-unsaturated porous media are now available.

4. SOIL CONSTITUTIVE MODELS

In order to reproduce soil behaviour under cyclic loading, as a sequence of loading–unloading–reloading, modifications have to be introduced to the classical constitutive models. The success for an elasto-plastic solution of the nonlinear coupled equations (22) depends on; firstly, a reasonable elasto-plastic constitutive model which can reproduce soil behaviour under complicated loading conditions and secondly, an accurate and stable integration algorithm for elasto-plastic constitutive relation. It is however imperative that the proposed model includes two characteristics. It must be in terms of effective stresses to show the failure when a residual angle of friction is reached and, it must be history dependent to show an accumulation of negative volumetric strain which results in pore pressure increases and hence strength degradation which is the essence of liquefaction. In addition, it should of course reproduce as accurately as possible stress-strain paths observed in laboratory experiments and make this with a relatively small number of parameters. In the present study, the nonlinear behaviour of soil is simulated for the description of cyclic loading using generalized plasticity theory based on the Pastor-Zienkiewicz (PZ), the Bolzon-Schrefler-Zienkiewicz (BSZ), and the enhanced-BSZ models.

The framework of generalized plasticity theory was first introduced by Zienkiewicz and Mroz [25] to model the behavior of sand under monotonic and cyclic loading. The main advantage of theory is that neither yield surface nor plastic potential surface needs to be explicitly defined. In generalized plasticity theory, the constitutive tensor in loading $\mathbf{C}_L^{-1} = \mathbf{D}_L$ differs from constitutive tensor in unloading $\mathbf{C}_U^{-1} = \mathbf{D}_U$, i.e. $d\boldsymbol{\varepsilon}_L = \mathbf{C}_L d\boldsymbol{\sigma}'$ for loading and $d\boldsymbol{\varepsilon}_U = \mathbf{C}_U d\boldsymbol{\sigma}'$ for unloading. In fact, at each point of the stress space, a direction tensor is specified to distinguish between loading and unloading. The constitutive matrix can be defined as

$$\mathbf{C}_L = \mathbf{C}^e + \mathbf{n}_{gL} \mathbf{n}_{gL}^T / H_L, \quad \mathbf{C}_U = \mathbf{C}^e + \mathbf{n}_{gU} \mathbf{n}_{gU}^T / H_U \quad (28)$$

or in reverse form

$$\mathbf{D}_L = \mathbf{D}^e - \frac{\mathbf{D}^e \mathbf{n}_{gL} \mathbf{n}_{gL}^T \mathbf{D}^e}{H_L + \mathbf{n}_{gL}^T \mathbf{D}^e \mathbf{n}_{gL}}, \quad \mathbf{D}_U = \mathbf{D}^e - \frac{\mathbf{D}^e \mathbf{n}_{gU} \mathbf{n}_{gU}^T \mathbf{D}^e}{H_U + \mathbf{n}_{gU}^T \mathbf{D}^e \mathbf{n}_{gU}} \quad (29)$$

where H_L and H_U are the plastic hardening/softening modulus in loading and unloading and \mathbf{n}_{gL} and \mathbf{n}_{gU} are the normal vector to plastic potential in loading and unloading

conditions. In this frame work, all necessary components of elasto-plastic constitutive matrix depend on the current state of stress and loading/unloading condition.

4.1 The Pastor-Zienkiewicz model

In the generalized plasticity framework of Pastor-Zienkiewicz model, parameters \mathbf{n}_g , \mathbf{n} and $H_{L/U}$ can be obtained without referring to plastic potential, or yield surfaces. However, the yield and potential surfaces, f and g , can be defined using the normal directions to these surfaces, as shown in Figure 1. In order to introduce the parameters of the model, a triaxial compression test may be applied. Considering $p' = J_1/3$ and $q = \sqrt{3J_{2D}}$ with their work-associated strains invariants ε_v^p and ε_s^p , it can be shown that the dilatancy d_g can be approximated from the stress ratio $\eta = p'/q$ as

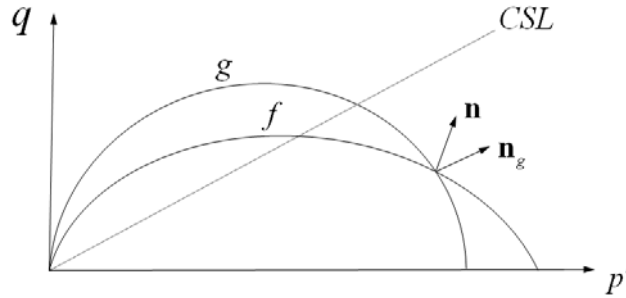


Figure 1. The yield and plastic potential surfaces of Pastor-Zienkiewicz model

$$d_g = \frac{d\varepsilon_v^p}{d\varepsilon_s^p} = (1 + \alpha)(M_g - \eta) \quad (30)$$

where α is the material parameter and M_g denotes the slope of critical state line. The normal vectors to the plastic potential and yield surfaces can be determined by

$$\mathbf{n}_g^T = (n_{gv}, n_{gs}) = (d_g, 1) / \sqrt{1 + d_g^2} \quad (31)$$

$$\mathbf{n}^T = (n_v, n_s) = (d_f, 1) / \sqrt{1 + d_f^2} \quad (32)$$

where d_f is defined in a similar manner to d_g by $d_f = (1 + \alpha)(M_f - \eta)$, where M_g/M_f is equal to relative density. If $d_f = d_g$, the hardening rule is associated.

The plastic modulus H_L for the loading condition is defined as

$$H_L = H_0 p' H_f (H_v + H_s) H_{DM} \quad (33)$$

where $H_f = (1 - \eta/\eta_f)^4$, $H_s = \beta_0 \beta_1 \exp(-\beta_0 \xi)$, $H_v = (1 - \eta/M_g)$, $H_{DM} = (\zeta_{\max}/\zeta)^\gamma$, $\eta_f = (1 + 1/\alpha)M_f$ and $\zeta = p'[1 - ((1 + \alpha)/\alpha)(\eta/M_g)]^{1/\alpha}$, with H_0 , β_0 , β_1 and γ_U denoting the material parameters obtained from experiments.

The plastic modulus H_U for unloading condition is defined as

$$\begin{aligned} H_U &= H_{U0} \left(M_g / \eta_U \right)^{\gamma_U} & \text{for } |M_g / \eta_U| > 1 \\ H_{U0} & & \text{for } |M_g / \eta_U| \leq 1 \end{aligned} \quad (34)$$

where H_{U0} is the material parameter and η_U is the stress ratio from which unloading takes place. The vector \mathbf{n}_{g_U} is defined as

$$\mathbf{n}_{g_U} = (n_{g_{Uv}}, n_{g_{Us}})^T = (-|n_{gv}|, +n_{gs})^T \quad (35)$$

4.2 The Bolzon-Schrefler-Zienkiewicz model

The BSZ model was proposed by Bolzon et al. [16] that considers the effective stress tensor and suction as independent stress variables. They have shown that the effective stress is thermodynamically consistent, and is particularly suitable for partially saturated soil mechanics compared with other stress tensors. Based on this model, the effective stress is defined as $\sigma'_{ij} = \sigma_{ij} + \delta_{ij}(S_w p_w + S_g p_g)$, with p_w and p_g are the water and gas pressures, respectively. Furthermore, the suction is defined by $s = p_c = p_g - p_w$, and the relationship between relative saturation and suction is assumed to be $S_r = 1 - m \tanh(\ell s)$ [10], where ℓ and m are material constants.

In BSZ model, the plastic behavior of soil is assumed as a function of suction by modifying the hardening modulus, defined in equation (33), through the introduction of multiplicative function \tilde{H}_w that relates the variation of hardening to suction linearly. i.e.

$$H_L = H_0 p' \tilde{H}_w H_f (H_v + H_s) H_{DM} \quad (36)$$

where $\tilde{H}_w = 1 + as$, with a denoting a material parameter. In this model, the function \tilde{H}_w is determined as required to fit different experimental data. In some cases, a dependence of \tilde{H}_w on p' has to be assumed to describe the behavior of soil that exhibit a maximum collapse at some value of the mean stress. This feature can be dealt with above relation by assuming the dependence of a on the effective mean stress p' through the function $a = a_1 \exp(-p') - a_2$. In this way, the original formulation of fully saturated soil can be recovered when suction is equal to zero.

Based on the dependence of plastic modulus on suction, similar description has been introduced in the yield and potential surface equations. Using the experimental observations [16], an increasing function of p_f on suction is assumed as $p_f = p'_{y0} + bs$, in which the

parameter b is determined by experimental data and p'_{y_0} is the initial yield stress for saturated condition.

4.3 The enhanced-BSZ model

The enhanced-BSZ model was proposed by Santagiuliana and Schrefler [21] by introducing a hydraulic constitutive relationship and a hydraulic hysteresis in the BSZ model to take into account the irreversible deformation during cyclic drying and wetting until structural collapse. In this model, the plastic strain is decomposed into two components; one depends on the effective stress tensor and the other on suction, i.e.

$$d\boldsymbol{\varepsilon}^p = \frac{1}{H} \mathbf{n}_g \mathbf{n}_g^T d\boldsymbol{\sigma}' + \frac{1}{H_b} \mathbf{n}_g ds \quad (37)$$

where

$$H_b = w H_0 p' \hat{H}_f \hat{H}_{DM} \quad (38)$$

with w denoting a parameter to be assumed as the function of suction. In above relation, $\hat{H}_f = (1 - \eta/\eta_f)$ and $\hat{H}_{DM} = (J(s)\zeta_{\max}/\zeta)^\gamma$, in which $J(s)$ provides an additional form of hardening due to partial saturation defined as $J(s) = \exp[\alpha(1 - S_w)]$, and the mobilized stress function is defined by $\zeta = p' [1 - (1/(1+c))(\eta/M)]^{1/c}$, where ζ_{\max} is the maximum value of ζ .

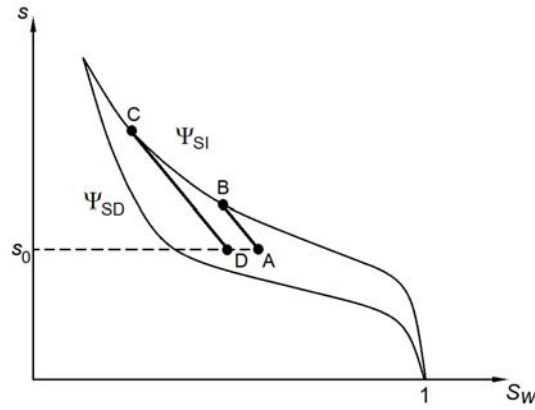
In this model, the wetting path is considered as an unloading stress path, and the first term of equation (37) is assumed zero. Thus,

$$d\boldsymbol{\varepsilon}_v^p = \frac{1}{w H_0 p' \hat{H}_f \hat{H}_{DM}} ds \quad (39)$$

It means that the plastic volume is proportional to the rate of suction, and implies that the model predicts the dilation of unsaturated soil when wetting occurs. In the plane of (s, S_w) , each cycle of drying and wetting has to be within two limiting curves obtained by drying from a fully saturated state Ψ_{SI} and wetting from a dry state Ψ_{SD} , as shown in Figure 2. These two functions link the suction to the degree of water saturation with an elasto-plastic relation that depends on water pressure. Santagiuliana and Schrefler [21] introduced two additional yield surfaces defining the elastic and elasto-plastic drying and wetting boundaries. These surfaces are denoted by the index SI for suction-increase (drying) yield surface and SD for the suction-decrease (wetting) yield surface. The new two surfaces SI and SD describe the irreversible changes in volume and degree of water saturation caused by cyclic drying and wetting under constant effective stress.

The elastic relationship between S_w^e and s is assumed to be linear as

$$dS_w^e = n K_s ds \quad (40)$$

Figure 2. The drying and wetting cycle in the plane of (s, S_w)

and the relationship between the plastic increment of S_w^p and the suction is defined as

$$dS_w^p = \left(\frac{1}{n} d\Psi_\alpha / ds - 1/K_s \right) ds \quad \alpha = \text{SI}, \text{SD} \quad (41)$$

5. VERIFICATION OF COMPUTATIONAL ALGORITHM

In order to evaluate and verify the performance of proposed computational algorithm, several examples are analyzed by means of a set of confining pressure and triaxial tests. The first three simulations include the drained behavior of a Hostun and certain loose and dense sands under compression in triaxial tests to illustrate the capability of PZ model. The next numerical example is chosen to demonstrate the validity of Bolzon-Schrefler-Zienkiewicz model for the behavior of partially saturated soil using the experiment performed on clay samples by Escario and Saez [26]. Finally, the behavior of enhanced-BSZ model is evaluated in the case of wetting and drying cycle using experimental data on compacted Bentonite-Kaolin. The convergence tolerance is set to 10^{-4} .

The first three-examples illustrate the evaluation of PZ model in numerical simulation of triaxial tests. A specimen of Hostun sand is numerically simulated under triaxial condition. Triaxial tests consisted of an initial isostatic compaction step up to pressure value of 207 MPa. The material parameters of PZ model for Hostun sand are given in Table 1. The variation of deviatoric stress with axial strain is presented in Figure 3(a). Also plotted in Figure 3(b) is the variation of volumetric strain with axial strain. Remarkable agreement can be observed between the proposed computational algorithm and those reported by Saada and Bianchini [27]. The next two examples are the simulation of two triaxial tests on certain loose and dense sands. The PZ material parameters for both sands are given in Table 2. Figure 4 presents the variation of deviatoric stress with axial strain for two different sands. There is a good agreement between the proposed model and those reported by Taylor [28].

Table 1: Hostun sand; the parameters of Pastor-Zienkiewicz model

K_0	G_0	M_g	M_f	α_g, α_f	β_0	β_1	H_0	γ, γ_U
43000.0	111000.0	1.26	1.2	0.45	2.0	0.13	1000.0	2.0

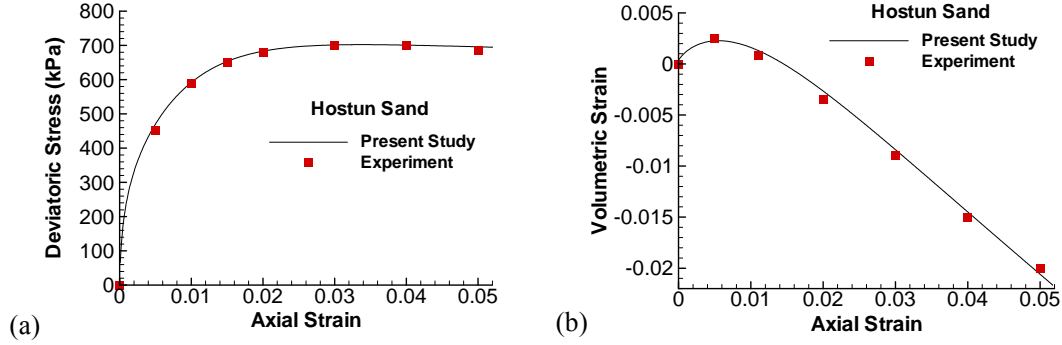


Figure 3. Drained behavior of Hostun Sand in compression triaxial test; a) The variation of deviatoric stress with axial strain, b) The variation of volumetric strain with axial strain

Table 2: The loose and dense sands; The parameters of Pastor-Zienkiewicz model

	K_0	G_0	M_g	M_f	α_g, α_f	β_0	β_1	H_0	γ, γ_U
Loose	30000.0	150000.0	1.33	0.50	0.45	2.25	0.2	4000.0	2.0
Dense	30000.0	150000.0	1.28	0.72	0.45	2.25	0.2	16000.0	2.0

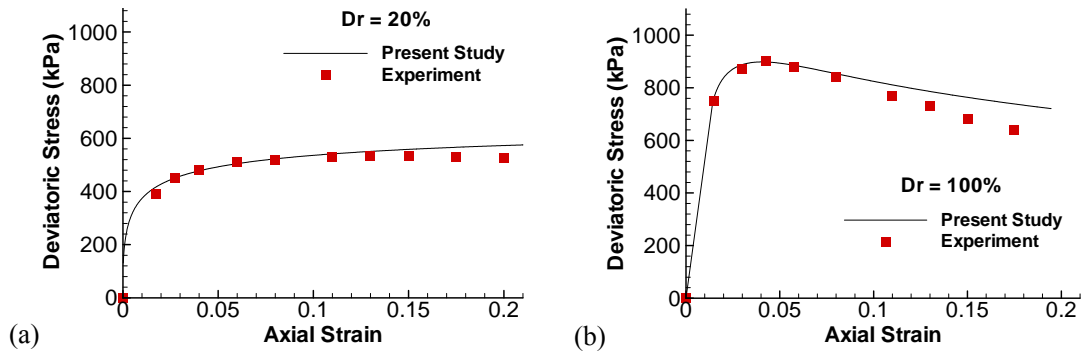


Figure 4. Drained behavior of loose and dense sands in compression triaxial test; a) Loose sand, b) Dense sand

In order to illustrate the performance of BSZ model, the behavior of partially saturated soil is investigated using the experimental test performed on clay sample. The material parameters of BSZ model for clay sample are given in Table 3. In Figure 5(a), the loading path is shown corresponding to the decrease of suction from 3.5 MPa to zero at constant vertical external pressure $\bar{p} = 0.2$ MPa, in which the material exhibits first swelling and then collapse. The wetting path (A \rightarrow B) in the planes of (\bar{p}, s) and (p', s) are shown by the solid and dashed lines, respectively. In Figure 5(b), the variation of predicted specific volume is plotted with suction. There is a good agreement between the proposed numerical simulation and that of experiment reported by Escario and Saez [26].

In the last example, the performance of enhanced-BSZ model is presented using an experiment test on compacted Betonite-Kaolin in the case of wetting and drying cycle. The material parameters of enhanced-BSZ model are given in Table 4. Suction first decreases from 200 kPa to 20 kPa and then, increases to 200 kPa at a constant mean net stress of 10 kPa. In Figure 6, the results of wetting-drying cycle on compacted Betonite-Kaolin are compared with those reported by Wheeler et al. [29] under isotropic stress-state in the planes of (s^*, p') , (v, s) and (S_r, s) . A comparison of the model predictions with experimental data illustrates that the proposed model successfully capture the elastic expansion during the wetting path and subsequently the irreversible compression during the drying path that does not exceed the maximum value of suction previously applied.

Table 3: Clay sample; The parameters of BSZ model

v_0	M	l	κ	$\lambda(0)$	a	p'_{y0}	i
2.3	0.8	2 MPa	0.035	0.0105	0.1 MPa ⁻¹	0.07 MPa	0.55

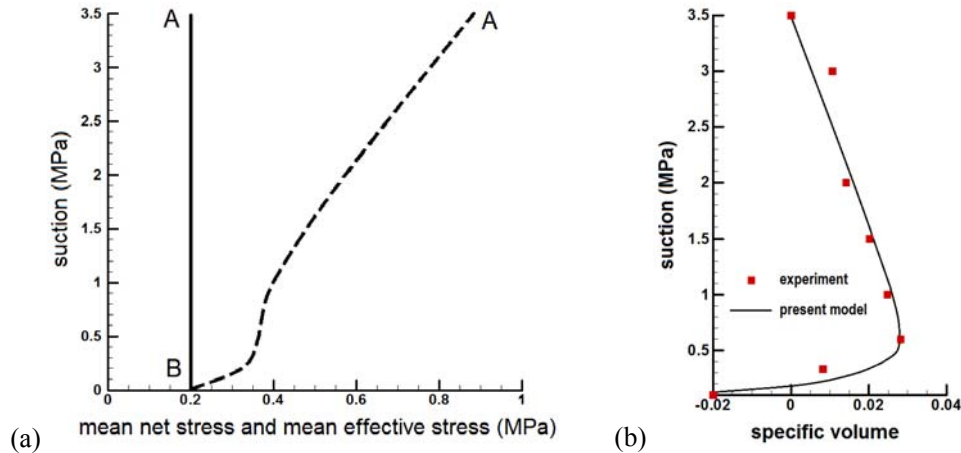


Figure 5. The partially saturated behavior of clay sample; a) The loading path in the planes of (\bar{p}, s) and (p', s) , b) The variation of predicted specific volume with suction

The Bolzon-Schrefler-Zienkiewicz model and enhanced-BSZ model have been used to simulate some important features of saturated-unsaturated soils, such as collapse due to suction and hydraulic hysteresis. These models define a yield surface in the plane of (p', s) , which can be used to model the collapse during wetting [16]. However, to simulate the situation that the confining stress and deviatoric stress change simultaneously, the modified Pastor-Zienkiewicz model based on the BSZ model is adopted here to simulate the failure of lower San-Fernando dam.

Table 4: The compacted Bentonite-Kaolin; The parameters of enhanced-BSZ model

v_0	S_r	$\lambda(0)$	κ	w	α	γ	S_D	S_I	A	p_{max}
2.2	0.65	0.15	0.02	10	8	10	200 kPa	2000 kPa	-0.003	20 kPa

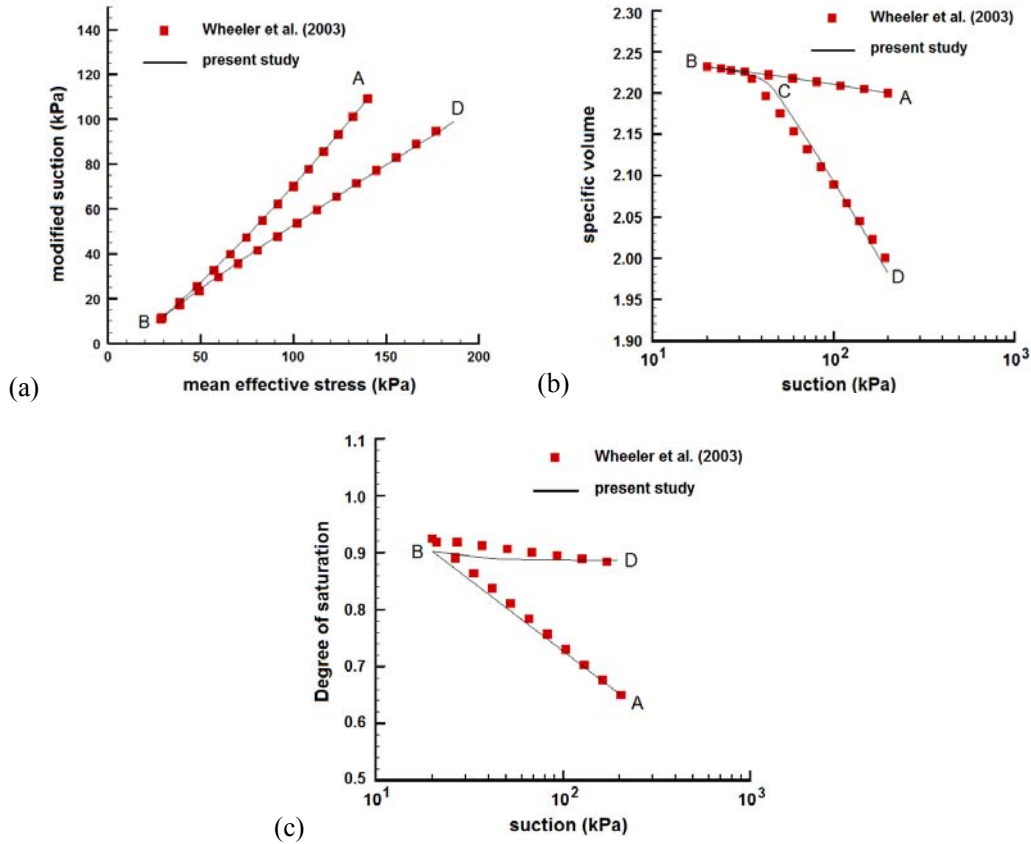


Figure 6. The wetting and drying cycle of compacted Bentonite-Kaolin under isotropic stress state; A comparison between the proposed simulation and experimental results in the planes: a) (s^*, p') , b) (v, s) , c) (S_r, s)

6. NUMERICAL MODELING OF LOWER SAN-FERNANDO DAM

In order to illustrate the capability of proposed computational algorithm in modeling of unsaturated porous media, the large FE deformation analysis of lower San-Fernando dam is presented under the 1971 earthquake using the modified PZ model. Numerical modeling is performed for 2D and 3D simulations and the results are compared. The analysis is carried out to simulate the failure of lower San-Fernando dam, which collapsed during the earthquake of February 9, 1971. Although the earthquake lasted for about 15 s, the failure of dam occurred at about 60 s after beginning of the earthquake. Seed et al. [30] illustrated this failure, as shown in Figure 7. They found that the time difference between the failure and end of the earthquake was due to important pore pressure build-up, as a result of cyclic loading, first in the central portion of the dam and then, the migration of this excess pore pressure in the post earthquake period to the regions closer to the upstream slope of the dam, and so the failure occurred at about 60 s after beginning of the earthquake.

The geometry, material zones and boundary conditions of the dam are shown in Figure 8. The finite element mesh employed in 3D simulation is eight-noded hexahedral elements with bilinear displacement interpolation and constant pressure. On the virtue of symmetry, the problem is modeled for one-half of the dam. The general material properties of the dam are given in Table 5 for different zones. The PZ material parameters are listed in Table 6. The relations between the degree of saturation, permeability and water pressure are plotted in Figure 9. The distribution of pore pressure in the dam body at steady state condition is presented in Figure 10(a) for 2D and 3D simulations. Obviously, the negative pore pressure exists in the dam crest and downstream slope in unsaturated zones. Without this suction the preliminary computations indicates that immediate local failure develops in dry material due to shaking. Figure 10(b) shows the distribution of effective vertical stress in the dam body at steady state condition. Good agreement can be observed between 2D and 3D simulations.

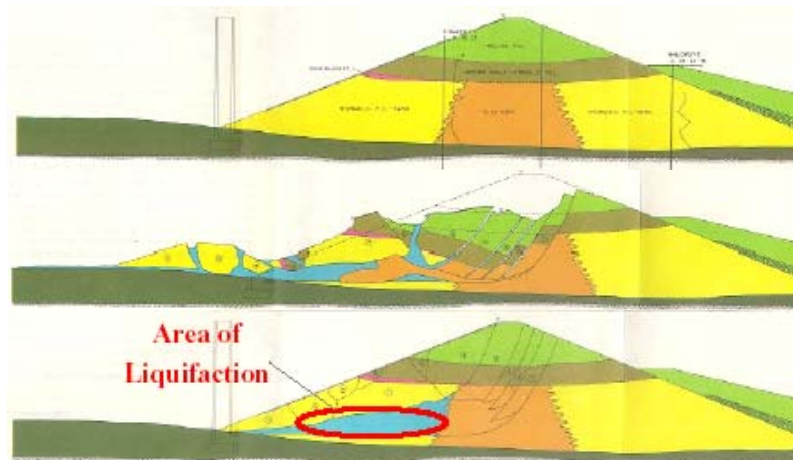


Figure 7. The mechanism of failure of the lower San-Fernando dam under the 1971 earthquake (Seed et al. [30])

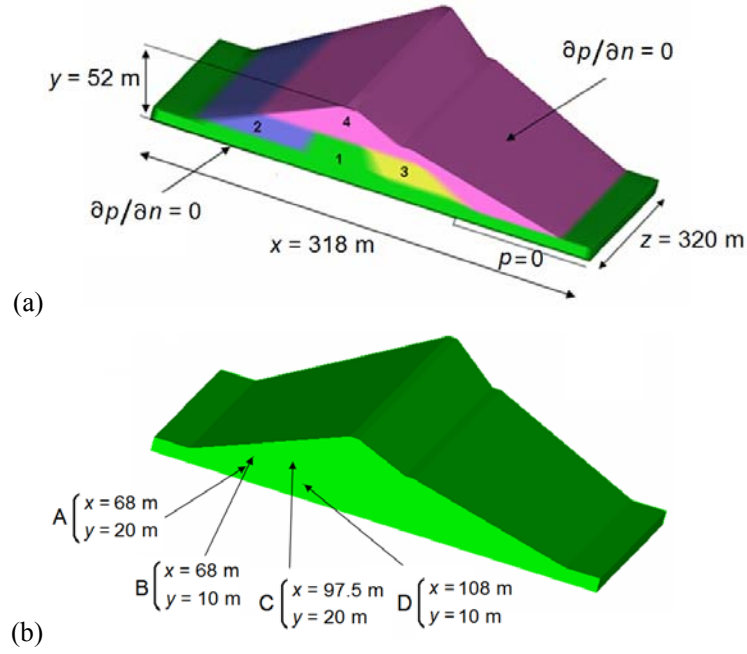


Figure 8. The material zones, geometry and boundary conditions of lower San-Fernando dam

Table 5: The San Fernando dam; The general material properties

Zone	E (Pa)	ν	K_s (Pa)	K_w (Pa)	ρ_s (kg/m ³)	N	k (m/s)
1	1.53e+8	0.2857	1.0e+22	2.0e+9	2756	0.375	0.001
2	0.89e+8	0.2857	1.0e+22	2.0e+9	2756	0.375	0.01
3	1.02e+8	0.2857	1.0e+22	2.0e+9	2756	0.375	0.001
4	0.98e+8	0.2857	1.0e+22	2.0e+9	2756	0.375	0.01

Table 6: The San Fernando dam; The parameters of modified Pastor-Zienkiewicz model

Zone	K_0	G_0	M_g	M_f	α_g, α_f	β_0	β_1	H_0	H_{u0} (Pa)	γ, γ_U	R_I	A (MPa ⁻¹)
1	120	180	1.55	1.400	0.45	4.2	0.2	700.0	6.00e+7	2.0	1.0	0.1
2	70	105	1.51	0.755	0.45	4.2	0.2	408.3	3.50e+7	2.0	1.0	0.1
3	80	120	1.51	1.133	0.45	4.2	0.2	467.0	4.00e+7	2.0	1.0	0.1
4	75	112	1.51	0.906	0.45	4.2	0.2	408.3	3.75e+7	2.0	1.0	0.1

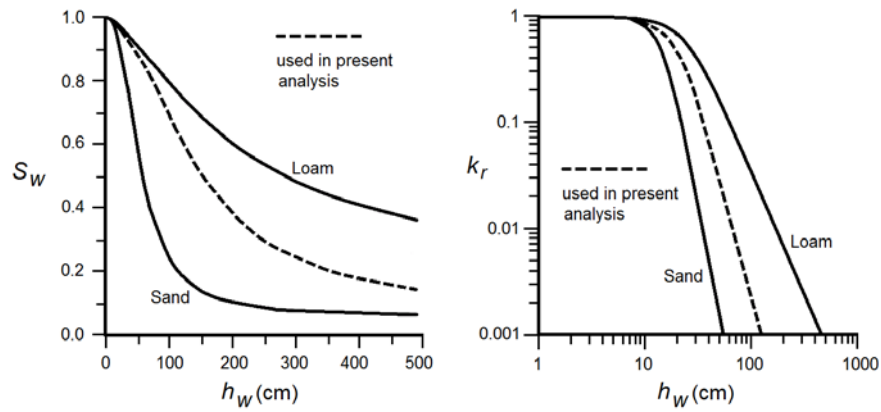


Figure 9. The relationships between pore-water pressure head $h_w = (p_w/\gamma_w)$, saturation S_w and relative permeability $k_r = k(S_w)/k(1)$ (after Huang and Zienkiewicz [24])

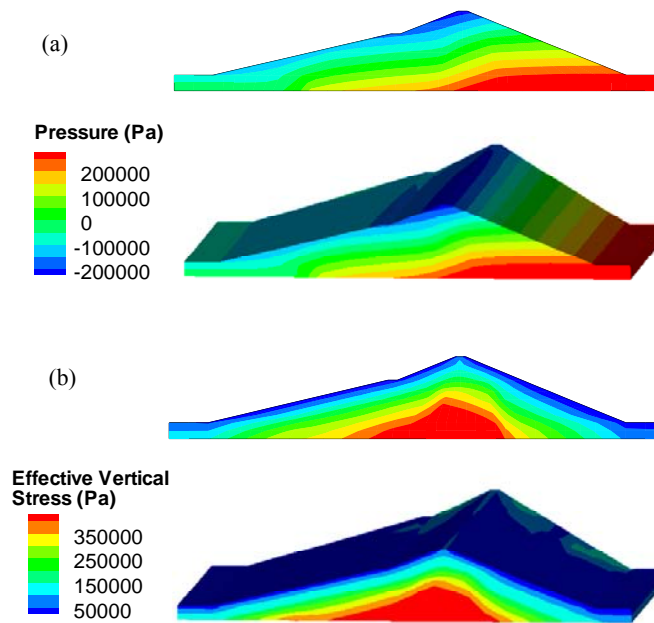


Figure 10. The steady state condition; a) The distribution of pore pressure, b) The distribution of effective vertical stress

The variations of excess pore pressure with time at different points are shown in Figure 11. A comparison between the 2D and 3D simulations is presented in this figure. As can be seen, the rate of dissipation of water pressure is similar in both analyses, however - the 3D analysis results in higher excess pore pressure. For all estimated points, 2D and 3D analyses predict the peak of excess pore pressure after the earthquake period. Furthermore, both simulations estimate the larger values of water pore pressures at the points near the upstream

slope in the center portion of the dam, i.e. points G and H. In Figure 12, the variations of horizontal and vertical displacements with time are presented at the dam crest and upstream slope (point G). It can be observed from the results of displacements on upstream slope that the model estimates the higher values of deformation in this region and thus, causes the failure in upstream slope near the center of the dam. Furthermore, the model predicts liquefaction in 60-90 s after beginning of the earthquake, which was experimentally reported by Seed et al. [30].

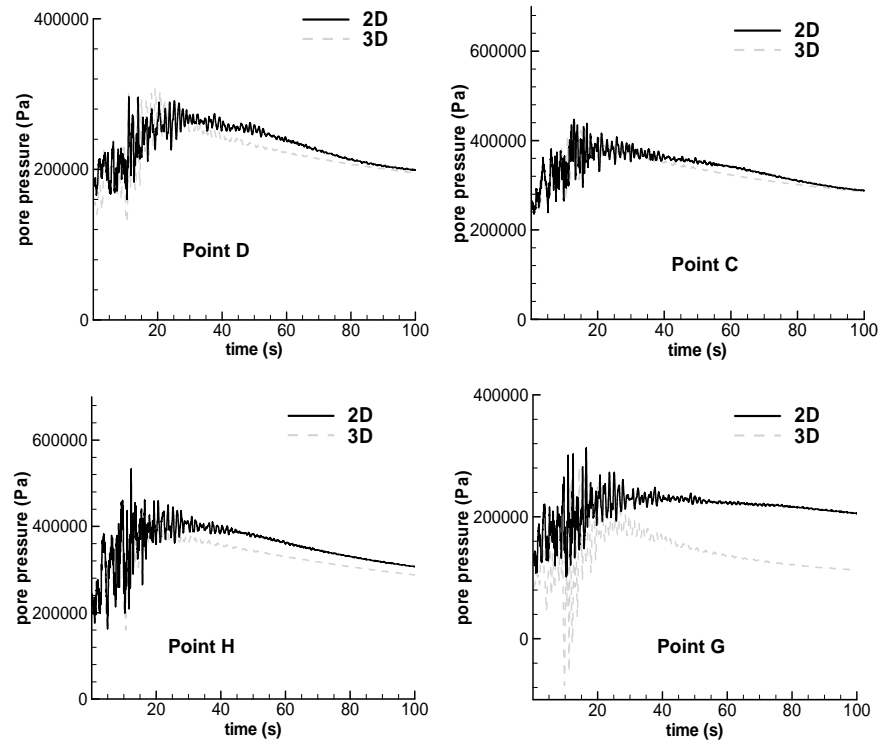


Figure 11. The variations of excess pore water pressure with time at different points

In order to illustrate the mechanism of the failure in the dam body, the distribution of excess pore water pressure, the effective stress contours, the distribution of first invariant of effective stress and the deformed meshes are presented in Figures 13 and 14 for 2D and 3D analyses at 15 and 60 s after beginning of the earthquake. According to Figure 13, there is a region with large portion of excess water pressure in the center of the dam at the end of earthquake. In Figure 14, the migration of this excess water pressure from the center portion of the dam into the upstream slope of the dam can be clearly observed. Also presented in this figure is the minimum values of the effective vertical stress and first invariant of effective stress in the upstream slope region, which is similar to the failure surface illustrated in Figure 7. These results demonstrate that there is a good agreement between the predicted failure using the modified Pastor-Zienkiewicz model and those reported by Seed et al. [30].

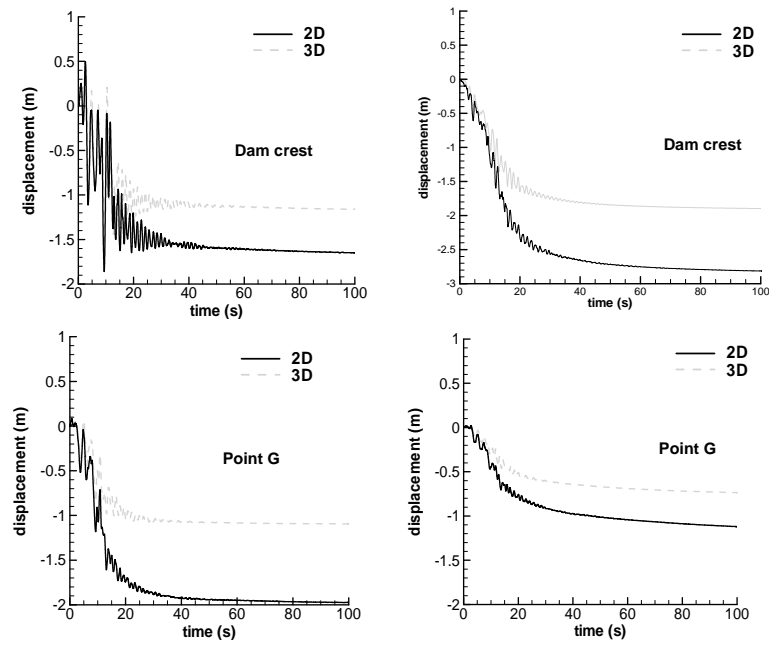


Figure 12. The variation of horizontal and vertical displacements with time at different points

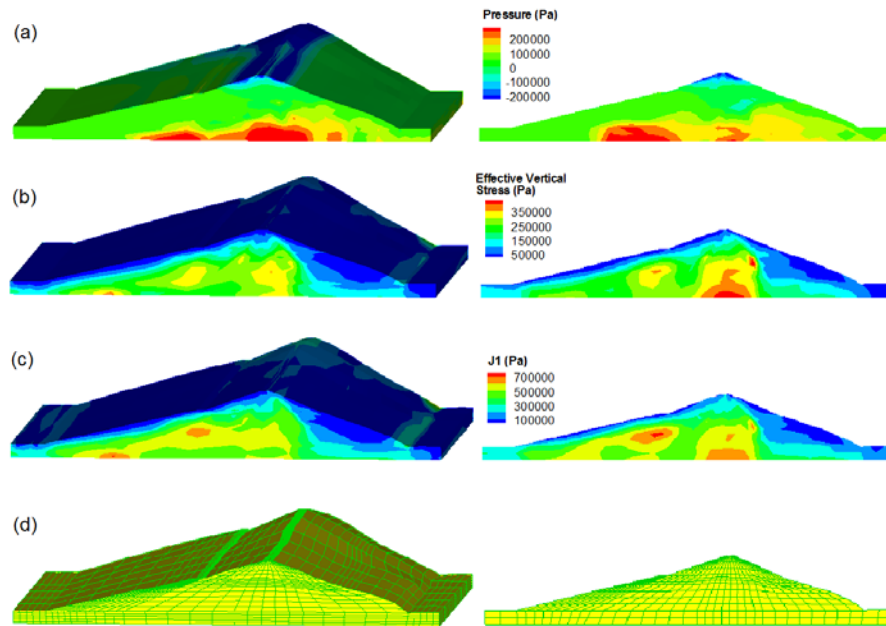


Figure 13. Numerical simulation results at 15.0 s after beginning of the earthquake for 2D and 3D modeling; a) The distribution of excess pore water pressure, b) The distribution of effective vertical stress, c) The distribution of first invariant of effective stress, d) The deformed mesh

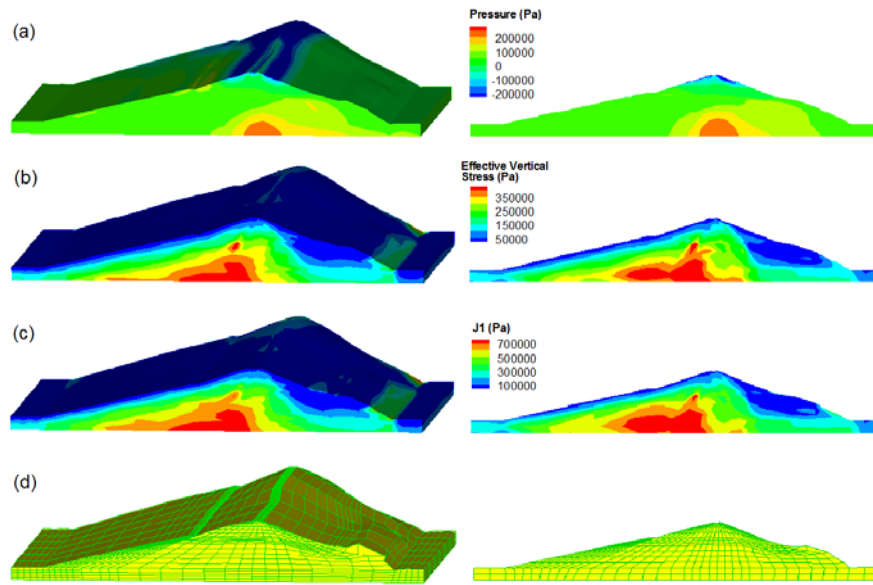


Figure 14. Numerical simulation results at 60.0 s after beginning of the earthquake for 2D and 3D modeling; a) The distribution of excess pore water pressure, b) The distribution of effective vertical stress, c) The distribution of first invariant of effective stress, d) The deformed mesh

7. CONCLUSION

In the present paper, the large plasticity deformation of 2D and 3D finite element simulation was presented for dynamic analysis of unsaturated soils with special reference to the failure of lower San Fernando dam under the 1971 earthquake. The coupled formulation based on Biot theory was presented for solving geotechnical problems associated with unsaturated soils. The large deformation Lagrangian FE formulation was applied to the governing equations for the spatial discretization, followed by a generalized Newmark scheme used for the time domain discretization. The framework of generalized plasticity was presented in the concept of three plasticity models, including: the Pastor-Zienkiewicz model, Bolzon-Schrefler-Zienkiewicz model, and the enhanced-BSZ model. The implementation of computational algorithm was validated by means of a set of confining pressure and triaxial tests, including: the drained behavior of a Hostun and certain loose and dense sands under compression in triaxial tests to illustrate the capability of PZ model, the partially saturated behavior of experiment performed on clay sample to demonstrate the validity of BSZ model, and the experiments of wetting and drying cycle on compacted Betonite-Kaolin to evaluate the behavior of enhanced-BSZ model. Finally, the modified Pastor-Zienkiewicz model was implemented to model the back analysis of the failure of lower San Fernando dam under the 1971 earthquake, and the comparison was performed between the 2D and 3D analyses. The results are shown that there is a good agreement between the predicted failure obtained by modified Pastor-Zienkiewicz model and those reported experimentally by Seed et al. [30].

Acknowledgements: The authors gratefully acknowledge the financial support of the Ministry of Energy, particularly Iran Water Resource Management Organization (IWRMO) through Grant No. 85/1751/100 awarded to Sharif University of Technology.

REFERENCES

1. Biot MA. Theory of propagation of elastic waves in a fluid-saturated porous solid. *Journal of the Acoustical Society of America*, **28**(1956) 168–91.
2. Biot MA. Mechanics of deformation and acoustic propagation in porous media. *Journal of Applied Physics*, **33**(1962) 1482–98.
3. Ghaboussi J, Wilson EL. Flow of compressible fluid in porous elastic media. *International Journal for Numerical Methods in Engineering*, **5**(1973) 419–42.
4. Zienkiewicz OC, Bettess P. Soils and other saturated media under transient dynamic conditions; General formulation and the validity of various simplifying assumptions. In: Pande GN, Zienkiewicz OC (Eds) *Soil Mechanics, Transient and Cyclic Loads*, Chapter 1, 1982.
5. Zienkiewicz OC, Shiomi T. Dynamic behavior of saturated porous media; The generalized Biot formulation and It's numerical solution. *International Journal for Numerical and Analytical Methods in Geomechanics*, **8**(1984) 71–96.
6. De Boer R, Kowalski SJ. A plasticity theory for fluid saturated porous media. *International Journal of Engineering Science*, **21**(1983) 11–16.
7. Zienkiewicz OC, Chan AHC, Pastor M, Paul DK, Shiomi T. Static and dynamic behavior of soils; A rational approach to quantitative solution, Part I. Fully saturated problems. *Proceedings of the Royal Society of London*, **429**(1990) 285–309.
8. Chang CS, Duncan JM. Consolidation analysis for partly saturated clay by using an elastic-plastic effective stress-strain model. *International Journal for Numerical and Analytical Methods in Geomechanics*, **7**(1983) 39–55.
9. Zienkiewicz OC, Xie YM, Schrefler BA, Ledesma A, Bicanic N. Static and dynamic behavior of soils; A rational approach to quantitative solution, Part II. Semi-saturated problems. *Proceedings of the Royal Society of London*, **429**(1990) 311–21.
10. Alonso EE, Gens A, Josa A. A constitutive model for partially saturated soils. *Geotechnique*, **40**(1990) 405–30.
11. Schrefler BA, Zhan X, Simoni L. A coupled model for water flow, airflow and heat flow in deformable porous media. *International Journal for Numerical Methods in Heat Fluid Flow*, **5**(1995) 531–47.
12. Gawin D, Schrefler BA. Thermo-hydro-mechanical analysis of partially saturated porous materials. *Engineering Computations*, **13**(1996) 113–43.
13. Li X, Thomas HR, Fan Y. Finite element method and constitutive modeling and computation for unsaturated soils. *Computer Methods in Applied Mechanics and Engineering*, **169**(1999) 135–59.
14. Schrefler BA, Scotta R. A fully coupled dynamic model for two-phase fluid flow in deformable porous media. *Computer Methods in Applied Mechanics and Engineering*, **190**(2001) 3223–46.

15. Pastor M, Zienkiewicz OC, Chan AHC. Generalized plasticity and the modeling of soil behavior. *International Journal for Numerical and Analytical Methods in Geomechanics*, **14**(1990) 151–90.
16. Bolzon G, Schrefler BA, Zienkiewicz OC. Elastoplastic soil constitutive laws generalized to partially saturated states. *Geotechnique*, **46**(1996) 279–89.
17. Simoni L, Salomoni V, Schrefler BA. Elastoplastic subsidence models with and without capillary effects. *Computer Methods in Applied Mechanics and Engineering*, **171**(1999) 491–502.
18. Schrefler BA, Zhang HW, Pastor M, Zienkiewicz OC. Strain localization modeling and pore pressure in saturated sand samples. *Computational Mechanics*, **22**(1998) 266–80.
19. Schrefler BA, Simoni L. An elastoplastic constitutive model for partially saturated soils. In: Lemaitre J (Ed) *Handbook of Material Behavior, Nonlinear Models and Properties*, Academic Press, San Diego, 2000.
20. Zhang HW, Heeres OM, de Borst R, Schrefler BA. Implicit integration of a generalized plasticity constitutive model for partially saturated soil. *Engineering Computations*, **18**(2001) 314–36.
21. Santagiuliana R, Schrefler BA. Enhancing the Bolzon–Schrefler–Zienkiewicz constitutive model for partially saturated soil. *Transport in Porous Media*, **65**(2006) 1–30.
22. Khoei AR, Azami AR, Haeri SM. Implementation of plasticity based models in dynamic analysis of earth and rockfill dams; A comparison of Pastor-Zienkiewicz and cap models. *Computers and Geotechnics*, **31**(2004) 385–410.
23. Khoei AR, Gharehbaghi SA, Azami AR, Tabarraie AR. SUT–DAM: An integrated software environment for multi-disciplinary geotechnical engineering. *Advances Engineering Software*, **37**(2006) 728–53.
24. Huang M, Zienkiewicz OC. New unconditionally stable staggered solution procedures for coupled soil-pore fluid dynamic problems. *International Journal for Numerical Methods in Engineering*, **43**(1998) 1029–52.
25. Zienkiewicz OC, Mroz Z. Generalized plasticity formulation and application to geomechanics. In: Desai CS, Gallagher RH (Eds) *Mechanics of Materials*, Wiley 1984, pp. 655–680.
26. Escario V, Saez J. Measurement of the properties of swelling and collapsing soils under controlled suction. *Proceedings of the 3rd International Conference on Expansive Soils*, Haifa, Academic Press, 1973, pp. 195–200.
27. Saada A, Bianchini G. *Constitutive Equations for Granular Non-cohesive Soils*, A.A. Balkema, Rotterdam 1989.
28. Taylor DW. *Fundamentals of Soil Mechanics*, John Wiley, New York 1948.
29. Wheeler SJ, Sharma RS, Buisson MSR. Coupling of hydraulic hysteresis and stress–strain behaviour in unsaturated soils. *Geotechnique*, **1**(2003) 41–54.
30. Seed HB. Consideration in the earthquake resistant design of earth and rockfill dams. *Geotechnique*, **29**(1979) 215–63.